Statistical Characteristics of Extreme Precipitation Events Over Tropical Oceans and Land Using Five Years of IMERG Data

Yaping Zhou[1,2], and Kuan-Man Xu[3]

1. UMBC/NASA Goddard Space Flight Center, Greenbelt, MD

2. Earth Resources Technology, Inc. College Park, MD

3. NASA Langley Research Center, Hampton, VA

Submitted to

Journal of Geophysical Research - Atmosphere

Corresponding author address:

Dr. Yaping Zhou

UMBC/NASA Goddard Space Flight Center, Greenbelt, MD

Earth Resources Corporation, Inc., Laurel, MD

Email: Yaping.Zhou@noaa.com

Key points:

1. We track 6.84 million tropical extreme precipitation events and analyze their duration, intensity, and size over land and ocean.
2. While 6–12 h events make up a higher percentage over land, 1–6 h events dominate both regions, with strong land-ocean diurnal differences.
3. Ocean events are larger/wetter at longer durations, while land events are stronger when short, reflecting distinct environmental controls.

Abstract

This study provides a statistical analysis of tropical extreme precipitation events (EPEs) using five years (2006-2010) of IMERG V06 Final Run data. EPE life cycles and spatial structures are tracked with a Lagrangian algorithm that allows spatial and temporal gaps and captures both light and heavy/extreme precipitation. Across the tropics, we identify 6.84 million EPEs (~3.99 million oceanic and ~2.85 million land) and examine their frequency and key characteristics, including duration, intensity, rainfall, and areal coverage, over tropical land and oceans. Geographic and seasonal patterns follow major convective regions, such as the ITCZ, with event counts migrating meridionally alongside the seasonal progression of tropical rainfall. Local event counts are dominated by 1–6-h events everywhere, while 6–12-h events make up a higher percentage over land. Diurnal cycles differ sharply: land EPEs peak in the afternoon, whereas oceanic events exhibit weaker morning and late-evening peaks. Substantial land-ocean contrasts also emerge in EPE properties. Oceanic 6–24-h events exhibit larger median and interquartile ranges of areal coverage, extreme rainfall, and total rainfall than their land counterparts, whereas for 1–6-h events the opposite holds. Relationships between areal coverage and total rainfall are broadly linear across several orders of magnitude, with upper bounds consistently larger over the ocean. Instantaneous attributes show similar linearity but greater scatter and comparable upper bounds across land and ocean, highlighting the role of duration in controlling rainfall. These results suggest that EPE characteristics are shaped by local environments and may respond differently to climate change over land and ocean.

Plain language summary

Extreme precipitation events (EPEs) can cause flooding, landslides, and major economic losses. Understanding how these events behave over tropical land and oceans is important for improving weather prediction and assessing future climate impacts. In this study, we analyzed five years of satellite rainfall data to track more than 6.8 million tropical EPEs. A tracking method was used that follows each event through time, even when rain temporarily weakens or shifts location. We found that 1–6-h duration events are the most common everywhere, but 6–12-h duration events make up a higher percentage over land. Over land, EPE counts peak in the afternoon when the surface heats up, while ocean events show much weaker daily variations. Land and ocean EPEs also differ in size and intensity. Over the ocean, longer events tend to cover larger areas and produce more total rainfall, while shorter events are generally stronger over land. The link between event size and total rainfall increases in a predictable way, although ocean events reach higher upper limits due to longer duration. Overall, the results show that extreme rainfall behaves very differently over land and ocean, suggesting that each environment may respond differently to future climate change.

1. Introduction

Current global climate models (GCMs) produce a weak increase ($2.52 \pm 0.22\%\ K^{-1}$, relative change) in global-mean precipitation with anthropogenic warming in comparison with the lower-tropospheric moisture increase (6.5–7% K^{-1}) (e.g., Allan et al., 2014; Fläschner et al., 2016; Oueslati et al., 2016). The low sensitivity of precipitation to warming relative to the moisture availability simulated by GCMs can be understood to arise from an energetic constraint (e.g., Newell et al., 1975; Mitchell et al., 1987; Stephens and Ellis, 2008; O'Gorman et al., 2012; Allan et al., 2014). However, the rate of increase in extreme (i.e., most intense) precipitation can exceed the moisture increase rate according to observations and GCM projections (e.g., Allan et al., 2014; Asadieh and Krakauer, 2015; O'Gorman, 2015; Fischer and Knutti, 2016; Myhre et al., 2019), especially in the deep Tropics (Norris et al., 2019). Studies have shown that the increase of total precipitation from extreme events with warming is not just determined by thermodynamic contributions (6.5–7% K^{-1}), but also further altered by dynamical contributions (e.g., Emori and Brown, 2005; Nie et al., 2018) and possibly by microphysical contributions (Bao et al., 2017; Da Silva et al., 2021). For example, amplification of large-scale ascent increases the vertical moisture transport while increases in the degree of convective aggregation may also impact extreme precipitation (Bao et al., 2017; Da Silva et al., 2021; Dai and Soden, 2020).

Convective aggregation resulting from complicated physical processes can be related to the changes in convective organization. An example of convective aggregation is humid clusters surrounded by dry patches simulated in idealized cloud-resolving models (CRMs). The mechanism for this instability is related to feedback among convection, moisture, clouds, radiation, and surface fluxes (e.g., Held et al., 1993; Bretherton et al., 2005; Muller and Held, 2012; Wing and Emanuel, 2014; Wing et al., 2017). CRM simulations revealed that daily precipitation extremes are related

to changes in the degree of convective aggregation, but instantaneous precipitation extremes are not affected by convective aggregation (Bao and Sherwood, 2019). However, Da Silva et al. (2021) used an adapted scaling analysis to show that instantaneous precipitation increases significantly with aggregation, mainly from microphysical contribution though increasing precipitation efficiency, while dynamic processes (convective drafts) decrease extreme precipitation in a warming climate. These results point to the need for an observational analysis of the complicated relationships of clouds, radiation, and extreme precipitation with dynamic and thermodynamic processes. A better understanding of the linkage of convective organization with dynamic processes can help to determine the sign of changes in extreme precipitation with global warming.

Most studies of extreme precipitation have focused two key characteristics: frequency and intensity, and they are often defined as the heaviest 1% or 5% of daily precipitation, computed at predefined temporal and spatial grids or at some gauge stations (e.g., Zhang et al., 2011; Trenberth et al., 2017; Myhre et al., 2019). Under this framework, changes in extreme precipitation amount can be decomposed into two parts, changes in frequency and changes in intensity. However, although convenient, the use of fixed grids does not capture an extreme precipitation event (EPE) as a coherent system, i.e., in a Lagrangian sense. Consequently, it cannot effectively detect long-term trends, because individual stations or small regions are unable to represent the evolving structure of EPEs, and the resulting signal is small relative to local natural variability (Myhre et al., 2019).

With the Eulerian framework, there is no information that details the duration, areal coverage, and total precipitation amount associated with an individual EPE. As a result, we cannot determine how these EPE attributes vary over time, how they contribute to local and regional precipitation accumulation, or how they change as the climate becomes warmer. Such attributes

116 can only be extracted from high tempo-spatial resolution data, such as the Integrated Multi-
117 satellitE Retrievals for GPM (IMERG) product from the U.S. Global Precipitation Measurement
118 (GPM) mission (Huffman et al. 2013, 2020). They cannot be reliably extracted from lower-
119 resolution gridded data sets or from rain gauge records.

120 The Lagrangian framework for identifying extreme precipitation has been widely adopted
121 (e.g., Chang et al., 2016; Davis et al., 2006; Ren et al., 2012; Skok et al., 2009, 2010, 2013).
122 Traditional precipitation-tracking algorithms, like their cloud tracking counterparts, follow heavy
123 precipitation features (e.g., > 2 mm h^{-1}) continuously in space and time with a fixed intensity
124 threshold. However, real precipitation systems can be organized yet discontinuous, causing the
125 fine structure of a localized heavy precipitation event to be fragmented into multiple small, short-
126 lived events. Zhou et al. (2019) addressed this issue using the high spatial-temporal resolution
127 IMERG dataset and a variable-threshold approach that permits spatial and temporal gaps in the
128 tracking and incorporates adjacent light-rain grids. Their method constructs EPEs in spatial-
129 temporal (xy-t) spaces that depict both the spatial extent and temporal evolution of extreme
130 precipitation systems. This algorithm enables an accurate depiction of each EPE's duration, areal
131 coverage, total rainfall, and propagation over its full life cycle. Using this algorithm, Zhou et al.
132 (2019) documented statistical characteristics of midlatitude EPEs over the contiguous United
133 States from April 2014 to March 2018.

134 The goal of this study is twofold: 1) to examine the statistical characteristics of event-based
135 precipitation extremes over the Tropics, extending the midlatitude EPE analysis of Zhou et al.
136 (2019) to tropical regions, and 2) to investigate the contrasts in the statistical characteristics
137 between tropical land and oceanic EPEs.

The rest of the paper is organized as follows. Section 2 describes the IMERG dataset, and the algorithm for extracting EPEs from IMERG dataset. Results are presented in Section 3. Summary and discussions are given in Section 4.

2. Dataset and methodology

2.1 The Integrated Multi-satellitE Retrievals for GPM (IMERG) dataset

The Integrated Multi-satellitE Retrievals for GPM (IMERG) is a high-resolution precipitation data set produced by the US GPM Science Team. It provides rainfall estimates at a spatial resolution of 0.1° × 0.1° and a temporal resolution of 30 minutes (Huffman et al., 2020). This dataset builds on the earlier Tropical Rainfall Measuring Mission (TRMM) Multi-satellite Precipitation Analysis (TMPA), which offered coarser resolutions of 0.25° × 0.25° and 3 hours and covered the latitudes from 50°S to 50°N (Huffman et al., 2010). In contrast, IMERG offers finer spatial-temporal detail and extends coverage to nearly entire globe.

The IMERG algorithm integrates precipitation estimates from an international constellation of passive microwave sensors abroad low Earth orbit satellites and infrared sensors abroad geosynchronous Earth orbit satellites. It also incorporates precipitation gauge analyses to provide crucial regionalization and bias correction for the satellite estimates. This enables the IMERG product to study the systematic dependence of precipitation frequency and intensity at resolutions that surpass those of previous datasets. The data period covers June 2000 to the present (Huffman et al., 2013, 2020), which includes the TRMM (2000-2015) period and the GPM period (2014 - present). In the present study, five years of data spanning from January 2006 to December 2010 are analyzed using the V06 Final Run dataset.

2.2 An algorithm for identifying extreme precipitation events (EPEs)

160 The EPE algorithm was developed by Zhou et al. (2019), which provided the rationales,
161 thresholds for extreme and light precipitation, and full algorithm details. Briefly, this algorithm
162 uses a recursive-fractal approach to connect all precipitating grids (>1 mm h^{-1}) across both space
163 and time that belong to the same system. It extends the object-oriented approach typically applied
164 to single snapshots (e.g., Mohr et al., 1999; Nesbitt et al., 2006; Liu et al., 2008; Xu et al., 2005)
165 into a continuous temporal dimension. This classification enables accurate depiction of the
166 duration, areal coverage, total rainfall, and propagation of an EPE over its entire lifecycle.
167 Specifically, the algorithm first identifies all extreme precipitating grids into an inventory,
168 from which the maximum extreme precipitating grid is found. Second, starting from this maximum
169 extreme precipitating grid, the algorithm recursively aggregates nearby extreme grids into an event
170 until no additional grids can be included. The included grids are then removed from the extreme
171 inventory to prevent them from appearing in another EPE. Third, the next maxima are identified
172 and organized into an event using the same aggregation method as the first event. In this way, the
173 events naturally expand in both spatial and temporal directions until the inventory is depleted.
174 Fourth, nearby light rain grids to an extreme grid in an event are included. At the conclusion of
175 each event, statistical properties and attributes of the EPEs are computed, as listed in Table 1. Note
176 that "fractal" here refers to how algorithm executes rather than the structure of derived events.
177 The derived EPEs depend upon the locally varying thresholds for light and extreme
178 precipitation and on the spatial and temporal gaps allowed in the algorithm. In the EPE algorithm
179 developed by Zhou et al. (2019), extreme grids are identified using local thresholds defined as the
180 greater of either the multi-year mean plus 2.5 times the standard deviation or 5 mm h^{-1}. Grids with
181 precipitation rates below 0.01 mm h^{-1} are excluded when computing the multi-year mean and
182 standard deviation. On the other hand, light rain grids are defined as those with precipitation rates

183 below the thresholds but above 1 mm h^{-1}. As discussed further below, gaps in both space and time
184 are allowed within an EPE, reflecting the fact that precipitation systems are organized yet often
185 spatially discontinuous and temporarily intermittent.

186 Figure 1 illustrates the locally varying thresholds used to identify extreme precipitation
187 grids, along with related variables across the tropics. The pattern of mean precipitation rate for the
188 precipitating grids for the period from July 2006 and June 2010 (Figure 1a) differ significantly
189 from the more familiar climatological mean, which usually includes non-precipitating grids
190 (Figure not shown) and the frequency of occurrence (Figure 1b). Mean precipitation rates are
191 typically 1.0-1.5 mm h^{-1} except for lower values observed over parts of the subtropical oceans,
192 northern Africa, the Arabic Peninsula, and parts of Australia.

193 As shown in Figure 1c, the extreme threshold is generally more than 5 times the mean
194 precipitation rate, though it is capped at 5 mm h^{-1} in regions where the mean precipitation rate is
195 below 1.0 mm h^{-1} (Figure 1a). The highest thresholds appear over land areas, rather than over
196 regions with the highest rainfall frequency such as the ITCZ, the Indian Ocean and the tropical
197 western Pacific (TWP) (Figure 1b). Overall, extreme precipitation accounts for less than 0.5% of
198 the total rainfall time over most of the Tropics (Figure 1d). The largest percentages occur in regions
199 with infrequent rainfall, such as northern Africa (Figure 1b), while percentages are far lower in
200 areas with frequent rainfall, such as the TWP. This indicates that the threshold is sufficiently
201 stringent to exclude moderate, long-duration rain events. Consequently, the fraction of time
202 classified as extreme remains relatively low in persistently rainy regions like the Indian Ocean and
203 the TWP (Figure 1d).

204 Allowing spatial and temporal gaps within an EPE is another key feature of the algorithm
205 developed by Zhou et al. (2019). Because the large-scale environments differ substantially

between the midlatitudes and the tropics, the gap settings used for midlatitude applications require adjustment for tropical conditions. Following Zhou et al. (2019), we assessed how the number of identified events responds to different choices of spatial and temporal gaps between extreme grids. For midlatitude EPEs over the contiguous U.S., Zhou et al. (2019) used a spatial gap of 50 km (~0.5°) and a temporal gap of 6 h, reflecting the fast propagation of precipitation systems in that region. For the tropics, smaller gaps are likely more appropriate. We found that the total number of events changes little when using a spatial gap of 0.1° with temporal gap of either 2 or 3 h, but declines more rapidly when larger spatial or temporal gaps are applied. Therefore, we adopted a spatial gap of 0.1° and a temporal gap of 3 h for extracting tropical EPEs. Further details of these sensitivity tests are provided in Section 3.1. For light-rain grids, the midlatitude gap settings — 0.2° in space and 2 h in time—are retained for tropical EPEs.

2.3 Individual EPE examples, attribute definitions, and algorithm implementation

Two examples of long-lasting tropical EPEs are shown in Figure 2 to illustrate the EPE algorithm. The first event occurred north of the equator over the Indian Ocean and lasted 73 hours, starting at 15 Z on January 18, 2007 (Figure 2a). The second was located along the South Pacific Convergence Zone (SPCZ) and lasted 30 hours, starting at 09 Z on January 5, 2007 (Figure 2b). Colors in the plots show the progression of time from the start (blue) to end (red) of each EPE.

The first EPE propagated northeastwards with an average speed of 9.5 m s^{-1}. It exhibited a clustered structure and weakened near the midpoint of its lifetime, then re-intensified as it merged with nearby convective systems before ending as a stationary precipitation cluster. The second EPE was quasi-stationary, oriented from northwest to southwest along the SPCZ. Additional panels (Figures 2c-e) show precipitation distributions during the early (13Z, January 5), peak (01 Z, January 6), and late (11 Z, January 6) stages of the event. This EPE started as scattered,

disconnected convective cells along the active SPCZ (Figure 2c), which gradually merged into a larger system that reached its maximum areal coverage around the midpoint of the event (Figure 2d). By the late stage, the system had decreased in size (Figure 2e). Over the 30-hour period, the system drifted northeastward, moving less than 200 km in total.

Some of the EPE attributes listed in Table 1 are self-explainable, while several others examined in this study are described here. The start and end times of each event are determined from the earliest and latest local times at which extreme precipitation occurs. Peak time can be defined in three ways: as the time of maximum precipitation intensity, maximum areal coverage, or maximum total rainfall. Throughout this study, including in Figure 2d, "peak time" specifically refers to the time of maximum areal coverage unless noted otherwise. The end time of an event may extend beyond the period of extreme precipitation. The term "event duration" is the time difference between the end and start times, whereas the "extreme duration" refers only to the portion of the event during which extreme precipitation occurs.

The total affected area, or areal coverage, is the sum of the areas of all grids that experience precipitation at any time during an event; thus, a grid contributes equally whether it rains once or over multiple hours. Precipitation depth is defined as the total accumulation at each grid point from both light and extreme precipitation over the entire event, from which spatial means and maxima are calculated across the affected grids. Instantaneous areal coverage, precipitation intensity, and rainfall are calculated hourly from both the extreme grids and all grids separately. Maximum and mean values of areal coverage, intensity, and rainfall are then derived from these time series. From the same time series, we also calculated the maximum extreme-to-total ratios for both rainfall and areal coverage.

At the onset of this study, we encountered several technical challenges in implementing the EPE algorithm due to the large volume of IMERG data and limitations in computer memory. The primary difficulty is that algorithm requires the full data record to be accessible in memory to extract EPEs across the spatial (x-y) and temporal (t) domains. In Zhou et al. (2019), this was addressed by loading one month of data at a time to produce multi-year EPE output over the contiguous U.S.. Temporal continuity between consecutive months was then enforced, allowing events at the end of one month to merge with those at the beginning of the next.

Because the tropical domain is substantially larger, we adopted a similar strategy but divided the full domain into three longitudinal subdomains: (1) the central and eastern Pacific (180°W-60°W, 27.5°S-27.5°N), (2) the Atlantic and Africa (60°W-60°E, 27.5°S-27.5°N), and (3) the Indian and western Pacific (60°E-180°E, 27.5°S-27.5°N), but still processing one month of data at a time. Spatial continuity was enforced across adjacent subdomains, allowing EPEs to extend across subdomain boundaries. Another key difference from Zhou et al. (2019) is that IMERG data were not used at its native 30-min resolution. Instead, they were aggregated to hourly intervals to accommodate the much larger study subdomains. This temporal binning may slightly affect the precise identification of EPE start, peak and end times, as well the delineation of EPE boundaries. However, it preserves the essential characteristics of most EPEs, making it suitable for statistical analysis.

3. Results

3.1 Sensitivity tests for spatial and temporal gaps

As discussed in Section 2.2, we assessed how the total number of extracted events respond to different combinations of spatial and temporal gaps applied to extreme precipitation grids. This analysis was performed for four representative months of the data record—January, April, July,

and October 2007—providing one month from each season. The rational is that the gap sizes appropriate for extracting midlatitude EPEs are likely too large for tropical EPEs, as tropical precipitation systems generally propagate more slowly. To further examine this sensitivity, we also stratified the event counts by both event duration and extreme duration. Given the pronounced land-ocean contrasts in convective behavior, results are presented separately for tropical land and oceanic regions.

Figure 3 shows the total numbers of extracted EPEs for five spatial (SP) and temporal (TP) gap combinations. The number following SP denotes the number of 0.1°× 0.1° grid boxes, and the number following TP indicates the number of hours. Using the midlatitude gap combination (SP5-TP6), we extracted 62,695 oceanic EPEs and 49,475 land EPEs. These totals increase by factors of 2-4 when smaller SP-TP gaps are applied, ranging from 159,251 to 277,213 oceanic EPEs and from 119,704 to193,414 land EPEs.

For a fixed spatial gap of 1, increasing TP from 2 to 3 decreases the event counts by 6.1% (ocean) and 3.4% (land). For a fixed spatial gap of 2, the same increase in TP decreases the event counts by 7.5% (ocean) and 4.9% (land). These reductions are modest, indicating limited sensitivity to TP for a fixed SP. However, increasing SP from 1 to 2 for a fixed TP (either 2 or 3 hours) cause event counts to drop by 37.9% (TP2) and 38.8% (TP3) for oceanic EPEs and 34.9% (TP2) and 36.0% (TP3) for land EPEs, respectively. Thus, the event totals are far more sensitive to SP than to TP.

To further explore these sensitivities, the total event counts are stratified by both event duration and extreme duration (Figure 4). For any SP-TP combination, event counts decrease exponentially with increasing extreme duration (Figures 4a and c). However, as event duration increases, the event counts increase slowly from 1 to 2 h, rise sharply from 2 to 3 h, and then

297 decreases exponentially thereafter (Figures 4b and d). Because a 2 h gap is permitted between
298 extreme and light rain grids, event duration may be up to 2 hours longer than extreme duration,
299 leading to more frequent 3-6 h events at the expense of 1-2 h events.

300 As either SP or TP increases, event counts decrease (Figure 3), primarily due to reductions
301 in short-duration EPEs (< 3 h extreme duration and < 6 h event duration), even though the number
302 of longer-duration events slightly increases (Figure 4). This pattern indicates that small, short-lived
303 events tend to be absorbed into nearby systems when the gaps are enlarged, while genuinely
304 independent events are largely unaffected. This behavior is especially pronounced when SP
305 increases from 1 to 2. Consistent with the total event counts (Figure 3), both EPE duration and size
306 (not shown) are more sensitive to SP than to TP, with larger gaps yielding larger and longer events
307 at the expense of smaller and shorter ones. This redistribution is particularly evident when
308 comparing the midlatitude SP-TP (SP5-TP06) combination with the four smaller-gap
309 combinations tested. The midlatitude combination produces substantially reduced event counts for
310 extreme durations of < 6 h over land and < 10 h over the ocean, and for event durations of < 10 h
311 over land and < 15 h over the ocean.

312 For the chosen gap combination (SP1-TP3), a total of 6,840,265 events are identified, of
313 which 68.5% over the ocean and 69.3% over land last less than 6 hours, while 28.5% of oceanic
314 events and 29.7% of land events last between 6 and 12 hours. EPEs lasting 12-24 hours account
315 for 2.70% of oceanic EPEs and 0.95% of land EPEs, while those exceeding 24 hours represent
316 only 0.33% of oceanic and 0.03% of land EPEs. The normalized percentage distributions indicate
317 that land exhibits a slightly higher fraction of events with durations between 3 and 12 h, but a
318 lower fraction of events shorter than 3 h and a substantially reduced occurrence of long-duration
319 events exceeding 12 h. In particular, the frequency of 12–18 h events over the ocean is

approximately 2.3 times greater than over land, while events lasting 24–48 h occur nearly an order of magnitude more frequently over the ocean than over land (Figures 4e and 4f).

3.2 Geographic distributions of five-year tropical EPE frequency and attribute

This section addresses the following questions. How are EPEs distributed across the tropics? Do their distributions follow the mean tropical rainfall patterns? What are the geographic variations in key EPE attributes such as intensity, areal coverage, depth and total rainfall for long-duration events (6–24 h)? How do intensity and depth vary for short-duration events (1–6 h)?

3.2.1 Seasonal variations of tropical EPE frequency

Over the five-year analysis period, a total of 6.84 million EPEs were identified, with 3.99 million occurring over the ocean and 2.85 million over land. Each event was assigned to a 5°×5° grid based on the longitude and latitude of its center (Table 1). Total event counts for each 5°×5° grid are shown for the four seasons—December-January-February (DJF), March-April-May (MAM), June-July-August (JJA), and September-October-November (SON)—in the left column of Figure 5. These counts are further separated by event duration into 1–6 h (2nd column), 6-12 h (3rd column), and longer than 12 h (right column) categories, representing approximately the bottom 69%, top 29%, and 2% of all events, respectively.

Although tropical land covers only ~28% of the tropical area, it contributes 42% of all EPEs. This imbalance partly explains why the consistently higher event counts over land compared to oceans except for longer than 12 h events, where the number of total events in this category is significantly low. For example, the number of 5°×5° grid cells with more than 800 events is substantially larger over land. This pattern holds for 98% of total events at duration ranges from 1-12 h (2nd and 3rd columns of Figure 5). As discussed later, two additional factors explain the

342 consistently higher event counts over land: 1) land EPEs tend to be smaller and shorter-lived than
343 oceanic events, and 2) their centers migrate more strongly with seasonal shifts in large-scale
344 circulation.

345 Consistent with the seasonal migration of the ITCZ and SPCZ and associated total rainfall
346 (Wu and Dickinson, 2003), EPE counts follow a pronounced meridional shift, moving northward
347 from austral (DJF) to boreal (JJA) summers and returning southward from JJA to DJF. This
348 migration contributes to the pronounced seasonal contrasts in event counts over land. During
349 boreal summer (JJA), EPEs occur frequently over North America and South Asia while South
350 America, South Africa, and Australia experience almost no events. The pattern reverses during
351 austral summer (DJF). During the transitional seasons (MAM and SON), event counts over South
352 America, South Africa, and Australia remain substantial but lower than in DJF. Over North
353 America and South Asia, more EPEs occur during SON than MAM, though both seasons exhibit
354 far fewer events than JJA. The higher SON activity may be related to a delayed seasonal decrease
355 in soil moisture as land surface cools (e.g., Betts, 2009).

356 Although mesoscale convective systems can persist over the ocean for extended periods
357 (Feng et al., 2021), Figure 5 shows that medium-long duration (6-12 h) EPEs are less frequent over
358 oceanic ITCZ regions than over land, but oceanic ITCZ does have comparable or higher frequency
359 of longer than 12 h events (last column, Figure 5 and Figure 4f). The medium and long-duration
360 events occur mostly over low-latitude land areas, including South America (except in JJA), the
361 TWP, the SPCZ and northern Asia (during JJA only). This suggests that only a small portion of
362 oceanic mesoscale systems produce extreme precipitation, even though such systems contribute
363 substantially to total rainfall over the oceans (e.g., Feng et al., 2021; Zhao, 2022). As discussed
364 later, oceanic EPEs may persist for more than a day and become more frequent than land-based

365 EPEs when aggregated over all 5° × 5° grids.

366 **3.2.2 Geographic distributions of annual-mean EPE attribute and frequency**

367 Annual-mean EPE attributes (Table 1) and frequencies are examined separately for
368 medium-long-duration (6–24 h; Figure 6) and short duration (1–6 h; Figure 7) events. We combine
369 the 12–24 h events with 6–12 h because of small number of events longer than 12 h. To better
370 represent their regional statistics, median and interquartile range (IQR) are used instead of means
371 and standard deviations, as many attributes exhibit large variability and non-Gaussian distributions
372 (Liu & Zipser, 2015). Attributes include areal coverage, total extreme rainfall, total rainfall,
373 maximum precipitation depth, and mean extreme-rainfall intensity (Figures 6c-i and 7c-i). Event
374 counts and their percentage contributions to all EPEs are shown in Figures 6a-b and Figures 7a-b.
375 A finer grid size (5°×2.5°) than that used for seasonal maps is chosen to ensure adequate sampling
376 and smoother spatial gradients.

377 High event counts for long-duration EPEs are observed along the ITCZ, particularly over
378 the Maritime Continent, the SPCZ, tropical Africa, and South America (Figure 6a). These regions
379 also show large percentage contributions (>30%; Figure 6b), consistent with frequent mesoscale
380 convective systems, Madan-Julian Oscillation (MJO; Madden & Julian, 1971, 1972) convection,
381 monsoonal rainfall, and tropical cyclones (Feng et al., 2021; Muhammad et al., 2021; Zhou et al.,
382 2013; Lau et al., 2008). The lowest EPE frequencies are found over subtropical oceanic subsidence
383 zones and certain inland continental regions.

384 Median areal coverage is largest over the equatorial oceans and toward the edges of the
385 Southern Hemisphere subtropics (Figure 6c), reflecting the influence of widespread cloud systems
386 embedded in tropical depressions, gigantic mesoscale convective complexes, monsoonal
387 circulations, and atmospheric rivers. Elevated median areal coverage and large IQRs also appear

388 in regions with very low EPE frequencies, such as the central Pacific, the area off the California
389 coast and the southern Indian Ocean (Figures 6a, 6c, 6d). These elevated values are linked to rare
390 but expansive systems such as MJO convective envelopes propagating into the central Pacific,
391 atmospheric rivers (the California coast), and intruding midlatitude cyclones (the southern Indian
392 Ocean). In these regions, light precipitation markedly increases areal coverage despite infrequent
393 occurrence of EPEs.

394 In contrast, both median and IQR of areal coverage are generally lower over many
395 continental regions (e.g., inland South Asia) and neighboring oceans, likely due to more localized
396 convection with shorter life cycles.

397 Spatial patterns of median extreme rainfall mirror those of areal coverage (Figure 6e).
398 Median total rainfall extends more broadly over oceanic and monsoon regions (Figure 6g) and is
399 typically 2–3 times larger, indicating that light rain significantly contributes to total precipitation.
400 Ocean-land contrasts in both median extreme and total rainfall are weaker than those seen from
401 areal coverage. Median maximum precipitation depth (maxDepth) is largest over the Bay of
402 Bengal, parts of the western Pacific, and coastal Central America and equatorial West Africa
403 (Figure 6i), likely due to prolonged localized heavy rainfall. Median mean extreme-precipitation
404 intensity (meanHR), which represents the average intensity over an entire EPE lifecycle, follows
405 a broadly similar geographical pattern but with broader maxima over land and slightly weaker
406 coastal enhancement (Figure 6j).

407 IQRs for cumulative attributes (areal coverage, extreme rainfall, and total rainfall) exceed
408 the median in most regions (Figures 6d, 6f, 6h), indicating substantial variability driven by
409 monsoons and ITCZ migration (Figure 5). As noted earlier, IQRs over land are much smaller than
410 over the ocean by a factor of 2-3. In contrast, IQRs for maxDepth and meanHR are closer to the

411 medians (Figures 6j, l), indicating that regional variability in cumulative attributes primarily arise
412 from differences in event duration rather than intensity.

413 Short-duration event counts are highest across the ITCZ, the Maritime Continent, the SPCZ,
414 the Amazon, and tropical Africa (Figure 7a). As expected, the percentage of short-duration EPEs
415 is largest in regions where all-duration EPEs are least common, such as the southeast Pacific,
416 southeast Atlantic, and northern Africa (Figure 7b).

417 Except for areal coverage over northern Africa, both the median values and IQRs of most
418 attributes are significantly higher over land than over the ocean (Figures 7e-l), although their
419 magnitudes are 1–2 orders of magnitude smaller than those of long-duration events. This land-
420 ocean contrast is opposite to that observed for long-duration EPEs. While the IQRs generally
421 exceed the medians, they usually remain within an order of magnitude, indicating that short-
422 duration events exhibit relatively less variability than longer-duration events. Variability is even
423 lower for maximum depth and mean intensity, particularly over land. Notably, the median mean
424 intensity is comparable to that of long-duration events, even though maximum depth is not.

425 **3.3 Contrasting the statistics of attributes between tropical land and oceanic EPEs**

426 Contrasts between oceanic and terrestrial environments are expected to influence EPE
427 characteristics, due to greater moisture availability over the ocean and stronger diurnal heating
428 over land (Nesbitt & Zipser, 2003; Yang & Slingo, 2001). Diurnal cycles of event counts are
429 composited using local event times (Table 1). Figure 8 shows the percentage of all EPEs occurring
430 in each hour of the day for the start, peak-volume, and end times for oceanic (blue) and land (red)
431 EPEs, where the peak-volume time refers to the hour with the maximum total rainfall.

432 Consistent with the weak diurnal cycle of oceanic convection, oceanic EPE counts exhibit
433 only modest diurnal variations. They show two weak peaks, one in the early morning for start time

434 at 09 h, peak time at 11 h, and end time at 13 h, and another in the late evening for start time at 23
435 h, peak time at 01 h, and end time at 04 h of next day, respectively. This weak diurnal cycle aligns
436 well with previous studies showing minimal diurnal variations in open-ocean convection (Yang &
437 Slingo, 2001; Tian et al., 2004).

438 In contrast, land EPE counts display a pronounced afternoon maximum, with onset, peak,
439 and end times at 13 h, 16 h, and 18 h, respectively, consistent with strong daytime heating and
440 afternoon convective initiation (Nesbitt & Zipser, 2003; Romatschke & Houze, 2010). The
441 amplitude of the diurnal variation spans ~2% of the daily total over the ocean and up to ~5% over
442 land, consistent with earlier findings of greater diurnal variability in terrestrial precipitation (Dai,
443 2001). For reference, a perfectly uniform distribution would allocate 4.167% of events per hour.

444 Large land-ocean differences also appear in several EPE attributes, due primarily to a
445 higher proportion of short-duration EPEs over land (Figures 6 and 7). Figure 9 shows joint
446 distributions of areal coverage versus event duration and total rainfall versus areal coverage for
447 tropical oceanic and land EPEs. As shown in Figure 4, for portions of the analysis period, event
448 counts decrease exponentially with event duration after peaking at around 6 h. The joint
449 distribution of areal coverage versus event duration reconfirms this earlier result. Over the ocean,
450 event counts associated with approximately median areal coverage (rather than all areal coverages
451 combined) drop by four orders of magnitude as event duration increases from 24 to 90 h—
452 approximately one order of magnitude per duration increment (24-35 h, 35-45 h, 45-60 h, 60-90
453 h). This result is consistent the scale-selective organization of tropical precipitation reported by
454 Mapes & Neale (2011). Over land, the same four-orders-of-magnitude decrease occurs over a
455 narrower duration range from 20 to 45 h, compared to 24 to 90 h over the ocean. This reconfirms
456 that EPE durations are generally shorter and extremely long-lived (> 24 h) events are rare over

lands, consistent with Romatschke & Houze (2010) and Houze (2012), who noted the transient nature of orographically and thermally forced convection.

Over both ocean and land, longer-duration events exhibit larger areas and larger total rainfall (Figure 9). However, these relationships show considerable spread: precipitation areas span 3 to 4 orders of magnitude for a given duration, and total rainfall spans by up to 2 orders of magnitude for a given area, despite the more linear relationship between total rainfall and areal coverage (Figures 9c, d), consistent with Liu & Zipser (2015). The upper bounds of these relationships are lower over land than ocean, implying that for a given duration, land EPEs produce smaller precipitation areas and consequently smaller total rainfall. These differences highlight a key contrast in precipitation efficiency—potentially influenced by moisture availability and vertical instability structure (Allan & Soden, 2008; Sahany et al., 2012).

Land-ocean contrasts are also evident in the instantaneous EPE attributes such as maximum hourly rainfall and areal coverage during an event, which exhibit generally linear relationships (Figures 10a, b), similar to those between total rainfall and areal coverage (Figure 9c, d). However, deviations from linearity span up to two orders of magnitude for oceanic EPEs at a fixed value of either maximum rainfall or areal coverage—slightly exceeding the deviations observed over land. Unlike the relationships involving total rainfall and areal coverage, the upper bounds of these instantaneous relationships are similar over ocean and land, suggesting that differences in event duration help explain the larger total rainfall and areal coverage observed over the ocean.

Maximum depths, which represent the highest precipitation accumulation at any grid point within an event, also show substantial variability with event duration, particularly for long-lived events. Local precipitation intensity, propagation speed, and event duration all influence maximum depth and contribute to the land–ocean contrasts illustrated in Figures 10c and 10d. Even at a fixed

480 event duration, the tails of maximum-depth distributions extend much farther for oceanic EPEs,
481 likely reflecting contributions from larger areas.

482 Overall, these land–ocean contrasts support the hypothesis that EPE characteristics are
483 governed by distinct local environments, implying that their responses to climate change may
484 diverge substantially between land and ocean regions (Dong et al., 2024; Pendergrass & Hartmann,
485 2014).

486 **4. Summary and discussions**

487 This study provides a comprehensive statistical analysis of tropical extreme precipitation
488 events (EPEs), using high-resolution precipitation data from IMERG. Unlike most previous work,
489 our approach takes a Lagrangian perspective, tracking the full life cycle of EPEs—including both
490 light and extreme precipitation. The algorithm we developed accommodates spatial and temporal
491 gaps not only between extreme precipitation grids but also between light and extreme precipitation
492 grids. We analyze the frequency of EPE occurrences over land and the ocean and key EPE
493 attributes such as duration, intensity, and areal coverage.

494 In this study, we have examined five years of IMERG V06 Final Run precipitation data
495 over the tropical belt (27.5°S-27.5°N) from January 2006 to December 2010. After assessing how
496 total event counts and their stratification by event duration and extreme duration respond to
497 different choices of spatial and temporal gaps applied to extreme precipitation grids, we have
498 selected a spatial gap of 0.1° and a temporal gap of 3 h. The algorithm has identified 6,840,265
499 EPEs in total: approximately 3.99 million over the ocean and 2.85 million over land. Of these,
500 68.5% of oceanic events and 69.3% of land events last less than 6 h, while 28.5% of oceanic events
501 and 29.7% of land events last between 6 and 12 hours. EPEs lasting 12-24 hours account for 2.70%
502 of oceanic EPEs and 0.95% of land events, while only 0.33% of oceanic and 0.03% of land EPEs

503 exceed 24 h. Land has a slightly higher percentage of events with durations of 3-12 h, whereas the
504 ocean has a slightly high percentage of events shorter than 3 h and a dominance of events lasting
505 longer than 12 h.

506 Geographic distributions and seasonal variations of event counts have been examined
507 separately for 1–6 h and 6–24 h duration categories, representing approximately the bottom 70%
508 and top 30% of all events. Most EPEs are observed over the ITCZ, the SPCZ, and summertime
509 continents, with higher land-based event counts across most duration categories except for >12 h
510 events. Their meridional migration follows the seasonal progression of the ITCZ and SPCZ from
511 austral (DJF) to boreal (JJA) summers and back, consistent with the seasonal cycle of tropical
512 rainfall (Wu and Dickinson, 2003). Although land EPEs remain prominent during the transitional
513 seasons, their occurrence is lower than in boreal or austral summer. Moreover, 6–24 h EPEs are
514 less frequent over the oceanic ITCZ than over land, suggesting that only a small subset of oceanic
515 mesoscale systems produce extreme rainfall, even though such systems contribute substantially to
516 total oceanic precipitation (e.g., Feng et al., 2021; Zhao, 2022).

517 Large land-ocean contrasts also appear in the geographic distribution of EPE attributes. For
518 6–24 h EPEs, median and interquartile range (IQR) of areal coverages, extreme rainfall, and total
519 rainfall are substantially higher over the ocean, whereas the opposite holds for 1–6 h events. These
520 results are consistent with the idea that oceanic environments favor more sustained and organized
521 convective systems (Romatschke & Houze, 2010; Liu & Zipser, 2015), while continental
522 convection is more localized and transient (Houze, 2012). Maximum depth and precipitation
523 intensity during an event tend to be higher over land regardless of duration—possibly due to
524 stronger convective updrafts over heated surfaces (Liu & Zipser, 2015). Both exhibit IQRs smaller

than their medians, whereas the opposite holds for cumulative attributes such areal coverage and total rainfall.

The aggregated tropical EPE statistics also reveal strong land-ocean contrasts. Over land, EPE counts display a pronounced afternoon peak, with onset, peak, and end times of 13 h, 16 h, and 18 h, respectively, consistent with strong daytime heating and afternoon convective initiation (Nesbitt & Zipser, 2003; Romatschke & Houze, 2010). Their diurnal amplitude exceeds the daily-mean hourly occurrence. Oceanic events show weaker diurnal variations with two modest peaks, one in the morning and another in the late evening—consistent with the minimal diurnal cycle of open-ocean convection (Nesbitt & Zipser, 2003; Tian et al., 2004; Yang & Slingo, 2001).

Event durations tend to be shorter over land, with very few extremely long-lived (> 12 h) events compared to over the ocean. Over both ocean and land, longer-duration events exhibit larger areal coverages and larger total rainfall. However, these relationships show considerable spread: areal coverages span 3 to 4 orders of magnitude for a given duration, and total rainfall spans by up to 2 orders of magnitude for a given area, despite the more linear relationships between areal coverage and total rainfall with smaller deviations (2 orders of magnitude in total rainfall and 1 order of magnitude in areal coverage). The upper bounds of these relationships are lower over land, implying that for a given duration, land EPEs produce smaller precipitation areas and consequently smaller total rainfall.

Instantaneous attributes such as maximum hourly rainfall and areal coverage during an event also exhibit approximately linear relationships, though with larger scatter. The upper bounds of these relationships, however, are similar between oceanic and land EPEs, suggesting that differences in event duration help explain the larger total rainfall and areal coverage observed over the ocean. These land-ocean contrasts may support the hypothesis that EPE attributes are governed

548 by distinct local environments, implying that their responses to climate change may diverge
549 substantially between land and ocean regions (Dong et al., 2024; Pendergrass & Hartmann, 2014).

550 In summary, tropical extreme precipitation events exhibit robust land–ocean contrasts in
551 their frequency, duration, spatial extent, and rainfall accumulation. While instantaneous
552 precipitation intensities are comparable over land and ocean, longer event durations and greater
553 spatial organization over the ocean largely explain the larger areal coverage and total rainfall of
554 oceanic events. These differences reflect fundamental contrasts in convective environments and
555 impose distinct upper bounds on event size and rainfall production, particularly over land. The
556 results underscore the importance of event life-cycle characteristics in shaping extreme
557 precipitation statistics and suggest that land and ocean extremes may respond differently to future
558 climate change.

559 Finally, some results may be influenced by the specifics of the EPE algorithm, given the
560 broad range of tropical extreme events—from isolated thunderstorms, mesoscale convective
561 systems, atmospheric rivers to fast-moving tropical cyclones. Although the algorithm is designed
562 to encompass all such events without excessive complexity, the selected spatial and temporal gaps
563 may not be suitable for every event type, and the flexible extreme-precipitation thresholds may be
564 restrictive in some regions or seasons. While the behavior of individual EPE attributes may be
565 sensitive to these factors, the aggregated statistical behaviors of tropical land and ocean EPEs and
566 their contrasts are unlikely to be significantly affected. A detailed discussion of algorithmic
567 limitations and their potential effects is provided in Zhou et al. (2019).

568 In future work, EPE attributes generated from this work will be matched with cloud and
569 radiative property data (Xu et al., 2023) and convective aggregation indices to study how

570 relationships among extreme precipitation, moisture, dynamics, convection, and radiation evolve
571 with convective aggregation and surface warming.
572
573
574 **Acknowledgments.** This work has been supported by NASA Science of Terra, Aqua, and NPP
575 program.
576
577 **Open Science.** The IMERG data were downloaded from NASA GES DISC (https://doi.org/
578 10.5067/GPM/IMERG/3B-HH/05). The extreme event statistics will be uploaded to
579 https://data.mendeley.com alongside with the database generated from previous extreme
580 precipitation events from Contiguous US.
581

582 References

583 Allan, R. P., & Soden, B. J. (2008). Atmospheric warming and the amplification of precipitation
584 extremes. Science, 321(5895), 1481–1484. https://doi.org/10.1126/science.1160787

585 Allan, R. P., Soden, B. J., John, V. O., Ingram, W., & Good, P. (2014). Current changes in
586 tropical precipitation. Environmental Research Letters, 9(12), 124002.
587 https://doi.org/10.1088/1748-9326/9/12/124002

588 Asadieh, B., & Krakauer, N. Y. (2015). Global trends in extreme precipitation: Climate models
589 versus observations. Hydrology and Earth System Sciences, 19(2), 877–891.
590 https://doi.org/10.5194/hess-19-877-2015

591 Bao, J., Sherwood, S. C., Alexander, L. V., & Evans, J. P. (2017). Future increases in extreme
592 precipitation exceed observed scaling rates. Nature Climate Change, 7, 128–132.
593 https://doi.org/10.1038/nclimate3201

594 Bao, J., & Sherwood, S. (2019). The relationship between convective aggregation and extreme
595 precipitation. Journal of Climate, 32(12), 4025–4042.

596 Betts, A. K. (2009). Land-surface-atmosphere coupling in observations and models, J. Adv.
597 Model. Earth Syst., 1, 4, doi:10.3894/JAMES.2009.1.4.

598 Bretherton, C. S., Blossey, P., and Khairoutdinov, M. (2005). An energy-balance analysis of
599 deep convective self-aggregation above uniform SST. *J. Atmos. Sci.,* **62,** 4273−4292.

600 Chang, W., Stein, M. L., Wang, J., Kotamarthi, V. R., & Moyer, E. J. (2016). Changes in
601 spatiotemporal precipitation patterns in changing climate conditions. Journal of Climate,
602 29(23), 8355–8376. https://doi.org/10.1175/JCLI-D-15-0844.1

603 Dai, A. (2001). Global precipitation and thunderstorm frequencies. Part II: Diurnal variations.
604 Journal of Climate, 14(6), 1112–1128. https://doi.org/10.1175/1520-
605 0442(2001)014<1112:GPATFP>2.0.CO;2

606 Dai, A., & Soden, B. J. (2020). Atmospheric convective aggregation and extreme precipitation.
607 Nature Climate Change, 10(3), 255–261.

608 Da Silva, N., Muller, C. J., & Frierson, D. M. (2021). Microphysical and dynamical
609 contributions to extreme precipitation trends. Geophysical Research Letters, 48(5),
610 e2020GL091976.

611 Davis, C., Brown, B., & Bullock, R. (2006). Object-based verification of precipitation forecasts.
612 Part I: Methodology and application to mesoscale rain areas. Monthly Weather Review,
613 134(7), 1772–1784. https://doi.org/10.1175/MWR3145.1

614 Dong, L., Chen, Y., & Wang, Y. (2024). Contrasting response of mesoscale convective systems
615 occurrence over tropical land and ocean to increased sea surface temperature.
616 Geophysical Research Letters, 51(4), e2024GL109251.
617 https://doi.org/10.1029/2024GL109251

618 Emori, S., & Brown, S. J. (2005). Dynamic and thermodynamic changes in mean and extreme
619 precipitation under changed climate. Geophysical Research Letters, 32(17), L17706.
620 https://doi.org/10.1029/2005GL023272

621 Feng, Z., Leung, L. R., Liu, N., Wang, J., Houze, R. A., Jr., Li, J., et al. (2021). A global high-
622 resolution mesoscale convective system database using satellite-derived cloud tops,
623 surface precipitation, and tracking. Journal of Geophysical Research: Atmospheres,
624 126(8), e2020JD034202. https://doi.org/10.1029/2020jd034202

625 Fischer, E. M., & Knutti, R. (2016). Observed heavy precipitation increase confirms theory and
626 early models. Nature Climate Change, 6, 986–991. https://doi.org/10.1038/nclimate3110

627 Fläschner, D., Mauritsen, T., & Stevens, B. (2016). Understanding the intermodel spread in
628 global-mean hydrological sensitivity. Journal of Climate, 29(2), 801–817.
629 https://doi.org/10.1175/JCLI-D-15-0351.1

630 Held, I. M., Hemler, R. S., & Ramaswamy, V. (1993). Radiative–convective equilibrium with
631 explicit two-dimensional moist convection. Journal of the Atmospheric Sciences, 50(23),
632 3909–3927. https://doi.org/10.1175/1520-0469(1993)050<3909:RCEWET>2.0.CO;2

633 Houze, R. A. (2012). Orographic effects on precipitating clouds. Reviews of Geophysics, 50(1).
634 https://doi.org/10.1029/2011RG000365

635 Huffman, G. J., Adler, R. F., Bolvin, D. T., & Nelkin, E. (2010). The TRMM Multi-satellite
636 Precipitation Analysis (TMPA). In *Satellite rainfall applications for surface hydrology,*
637 F. Hossain and M. Gebremichael (Eds.), Springer Verlag, pp. 3–22.

638 Huffman, G. J, Bolvin, D. T., Braithwaite, D., Hsu, K., Joyce, R., & Xie, P. (2013). NASA
639 Global Precipitation Measurement Integrated Multi-satellitE Retrievals for GPM
640 (IMERG). NASA Algorithm theoretical basis document (ATBD) version 4.1. [23]

641 Huffman G. J., Bolvin, D. T., Braithwaite, D., et al., (2020). Integrated multi-satellite retrievals
642 for the Global Precipitation Measurement (GPM) mission (IMERG). In *Satellite*
643 *Precipitation Measurement*, Springer: Cham, Switzerland, pp. 343–353.

644 Lau, W. K., Zhou, Y., & Wu, H. (2008). Have tropical cyclones been feeding more extreme
645 rainfall? Journal of Geophysical Research: Atmospheres, 113(D23), D23113.
646 https://doi.org/10.1029/2008JD009963

Liu, C., Zipser, E. J., Cecil, D. J., Nesbitt, S. W., & Sherwood, S. (2008). A cloud and precipitation feature database from nine years of TRMM observations. *J. Appl. Meteor. Climatol.,* **47**, 2712–2728, doi:10.1175/2008JAMC1890.1.

Liu, C., & Zipser, E. J. (2015). The global distribution of largest, deepest, and most intense precipitation systems. *Geophys. Res. Lett.*, 42, 3591–3595. doi: 10.1002/2015GL063776.

Madden, R., & Julian, P. (1971). Detection of a 40-50 day oscillation in the zonal wind in the tropical Pacific, J. Atmos. Sci., 28, 702-708.

Madden, R., & Julian, P. (1972). Description of global-scale circulation cells in the tropics with a 40-50 day period. J. Atmos. Sci., 29, 1109-1123.

Mapes, B. E., & Neale, R. B. (2011). Parameterizing convective organization to escape the entrainment dilemma. Journal of Climate, 24(16), 4487–4495. https://doi.org/10.1175/JCLI-D-10-00124.1

Mitchell, J. F. B., Wilson, C. A., & Cunnington, W. M. (1987). On CO_2 climate sensitivity and model dependence of results. Quarterly Journal of the Royal Meteorological Society, 113(475), 293–322. https://doi.org/10.1002/qj.49711347517

Mohr, K. I., Famiglietti, J. S., & Zipser, E. J. (1999). The contribution to tropical rainfall with respect to convective system type, size, and intensity estimated from the 85 GHz ice scattering signature. Journal of Applied Meteorology, 38(5), 596–606. https://doi.org/10.1175/1520-0450(1999)038<0596:TCTTRW>2.0.CO;2

Muhammad, F. R., Lubis, S. W., & Setiawan, S. (2021). The influence of boreal summer Madden-Julian Oscillation on precipitation extremes in Indonesia. arXiv. https://arxiv.org/abs/2112.00001

Muller, C. J., & Held, I. M. (2012). Detailed investigation of the self-aggregation of convection in cloud resolving simulations. Journal of the Atmospheric Sciences, 69(8), 2551–2565. https://doi.org/10.1175/JAS-D-11-0257.1

Myhre, G., K. Alterskjær, C. W., Stjern, C. W., et al., 2019: Frequency of extreme precipitation increases extensively with event rareness under global warming. *Sci. Rep.,* **9,** 16063, doi:10.1038/s41598-019-52277-4.

Nesbitt, S. W., & Zipser, E. J. (2003). The diurnal cycle of rainfall and convective intensity according to three years of TRMM measurements. *Journal of Climate*, **16**(10), 1456–1475. **https://doi.org/10.1175/1520-0442-16.10.1456**

Nesbitt, S. W., Cifelli, R., & Rutledge, S. A. (2006). Storm morphology and rainfall characteristics of TRMM precipitation features. *Mon. Wea. Rev.,* **134**, 2702–2721, doi:10.1175/MWR3200.1.

Newell, R. E., Newell, N. E., Zhu, Y., & Scott, C. (1975). Tropospheric rivers?—A pilot study. Geophysical Research Letters, 19(3), 2401–2404.

Nie, J., Sobel, A. H., Shaevitz, D. A., & Wang, S. (2018). Dynamic amplification of extreme precipitation sensitivity. *PNAS,* **115**, 9467-9472, doi:10.1073/pnas.1800357115.

Norris, J. R., Allan, R. P., Evan, A. T., Zelinka, M. D., O'Dell, C. W., & Klein, S. A. (2019). Evidence for climate change in the satellite cloud record. Nature, 536(7614), 72–75. https://doi.org/10.1038/nature18273

O'Gorman, P. A. (2015). Precipitation extremes under climate change. Current Climate Change Reports, 1, 49–59. https://doi.org/10.1007/s40641-015-0009-3

O'Gorman, P. A., Allan, R. P., Byrne, M. P., & Previdi, M. (2012). Energetic constraints on precipitation under climate change. *Surv. Geophys.*, **33**, 585–608, doi:10.1007/s10712-011-9159-6.

Oueslati, B., Bony, S., Risi, C., & Dufresne, J.-L. (2016). Interannual variability of monsoon precipitation: A CMIP5 model intercomparison. Climate Dynamics, 47(7–8), 2271–2290. https://doi.org/10.1007/s00382-015-2963-9

Pendergrass, A. G., & Hartmann, D. L. (2014). The atmospheric energy constraint on global-mean precipitation change. Journal of Climate, 27(2), 757–768. https://doi.org/10.1175/JCLI-D-13-00163.1

Ren, F., Cui, D., Gong, Z., Wang, Y., Zou, X., Li, Y., et al. (2012). An objective identification technique for regional extreme events. Journal of Climate, 25(20), 7015–7027. https://doi.org/10.1175/JCLI-D-11-00489.1

Romatschke, U., & Houze, R. A. (2010). Characteristics of precipitating convective systems in the South Asian monsoon. Journal of Hydrometeorology, 11(1), 3–20. https://doi.org/10.1175/2009JHM1289.1

Sahany, S., Neelin, J. D., Hales, K., & Ryu, J. H. (2012). Temperature–moisture dependence of the deep convective transition as a constraint on entrainment in climate models. Journal of Climate, 25(14), 4445–4468. https://doi.org/10.1175/JCLI-D-11-00137.1

Skok, G., Bacmeister, J., & Tribbia, J. (2013). Analysis of tropical cyclone precipitation using an object-based algorithm. Journal of Climate, 26(8), 2563–2579. https://doi.org/10.1175/JCLI-D-12-00135.1

Skok, G., Tribbia, J., & Rakovec, J. (2010). Object-based analysis and verification of WRF model precipitation in the low- and midlatitude Pacific Ocean. Monthly Weather Review, 138(12), 4561–4575. https://doi.org/10.1175/2010MWR3472.1

Skok, G., Tribbia, J., Rakovec, J., & Brown, B. (2009). Object-based analysis of satellite-derived precipitation systems over the low- and midlatitude Pacific Ocean. Monthly Weather Review, 137(10), 3196–3218. https://doi.org/10.1175/2009MWR2900.1

Stephens, G. L., & Ellis, T. D. (2008). Controls of global-mean precipitation increases in global warming GCM experiments. *J. Climate,* **21***,* 6141-6155, doi:10.1175/2008JCLI2144.1.

Tian, B., Soden, B. J., a& Wu, X. (2004). Diurnal cycle of convection, clouds, and water vapor in the tropical upper troposphere: Satellites versus a general circulation model, *J. Geophys. Res.*, **109**, D10101, doi:**10.1029/2003JD004117**.

Trenberth, K. E., Zhang, Y., & Gehne, M. (2017). Intermittency in precipitation: Duration, frequency, intensity, and amounts using hourly data. Journal of Hydrometeorology, 18(5), 1393–1412. https://doi.org/10.1175/JHM-D-16-0263.1

Wing, A. A., & Emanuel, K. A. (2014). Physical mechanisms controlling self-aggregation of convection in idealized numerical modeling simulations. *J. Adv. Model. Earth Syst.,* **6,** 59-74.

Wing, A. A., & Cronin, T. W. (2016). Self-aggregation of convection in long channel geometry. *Quart. J. Roy. Meteor. Soc.*, **142***,* 1–15, doi:10.1002/qj.2628.

Wing, A. A., Emanuel, K. A., Holloway, C. E., & Muller, C. (2017). Convective self-aggregation in numerical simulations: A review. *Surv. Geophys.,* **38,** 1173−1198.**Wu, R., and R. E. Dickinson, 2003**: Warm-season rainfall variability over the tropical Pacific and Atlantic. *Journal of Climate*, **16**, 382–401.

Xu, K.-M., Wong, T., Wielicki, B. A., Parker, L., & Eitzen, Z. A. (2005). Statistical analyses of satellite cloud object data from CERES. Part I: Methodology and preliminary results of 1998 El Nino/2000 La Nina. *J. Climate,* **18,** 2497-2514.

Xu, K.-M., Zhou, Y., Sun, M., Kato, S., & Hu, Y. (2023). Observed cloud type-sorted cloud property and radiative flux changes with the degree of convective aggregation from CERES data. Journal of Geophysical Research: Atmospheres, 128, e2023JD039152. https://doi.org/10.1029/2023JD039152

Yang, G. Y., & Slingo, J. (2001). The diurnal cycle in the Tropics. Monthly Weather Review, 129, 784-801. https://doi.org/10.1175/1520-0493(2001)129<0784:TDCITT>2.0.CO;2

Zhang, X., Alexander, L., Hegerl, G. C., Jones, P., Klein Tank, A., Peterson, T. C., et al. (2011). Indices for monitoring changes in extremes based on daily temperature and precipitation data. WIREs Climate Change, 2(6), 851–870. https://doi.org/10.1002/wcc.147

Zhao, M., (2022). A study of AR-, TS-, and MCS-associated precipitation and extreme precipitation in present and warmer climates. *J. Climate,* **35**, 479–497.

748 Zhou, Y., Lau, W. K., & Liu, C. (2013). Rain characteristics and large-scale environments of
749 precipitation objects with extreme rain volumes from TRMM observations. Journal of
750 Geophysical Research: Atmospheres, 118(17), 9673–9689.
751 https://doi.org/10.1002/jgrd.50776

752 Zhou, Y., Nelson, K., Mohr, K. I., Huffman, G. J., Levy, R., & Grecu, M. (2019). A spatial-
753 temporal extreme precipitation database from GPM IMERG. Journal of Geophysical
754 Research: Atmospheres. https://doi.org/10.1029/2019jd030449

755

Table 1. List of extreme precipitation event attributes. Maximum and mean values are derived from the time series of instantaneous quantities, except for precipitation depth. "Total" refers to the accumulation over the entire event. The number of parameters and the unit for each attribute are given in parenthesis. See text for details.

Parameter	Explanation
Time (4, UTC)	Start, peak, and end times of the entire system and end time with extreme precipitation
Duration (2, hour)	The time span of the entire system and the time span with extreme precipitation only
Location (2, degree)	Longitude and latitude of precipitation intensity-weighted center
Total amount (4, m^3)	Accumulated precipitation amounts from extreme and all precipitating grids of the entire system (total and maximum)
Areal coverage (2, km^2)	Precipitation affected area (total and maximum)
Intensity (2, mm h^{-1})	Precipitation intensity (total amount divided by areal coverage) of the entire system (mean and maximum)
Depth (2, mm)	Precipitation received at grids over precipitation affected area during the event (spatial mean and maximum)
Extreme-to-total ratio (2)	Instantaneous extreme-to-total ratios in total amount of precipitation and areal coverage (maximum)
Propagation speed (4, m s^{-1})	Speeds in horizontal and meridional directions (mean and maximum)

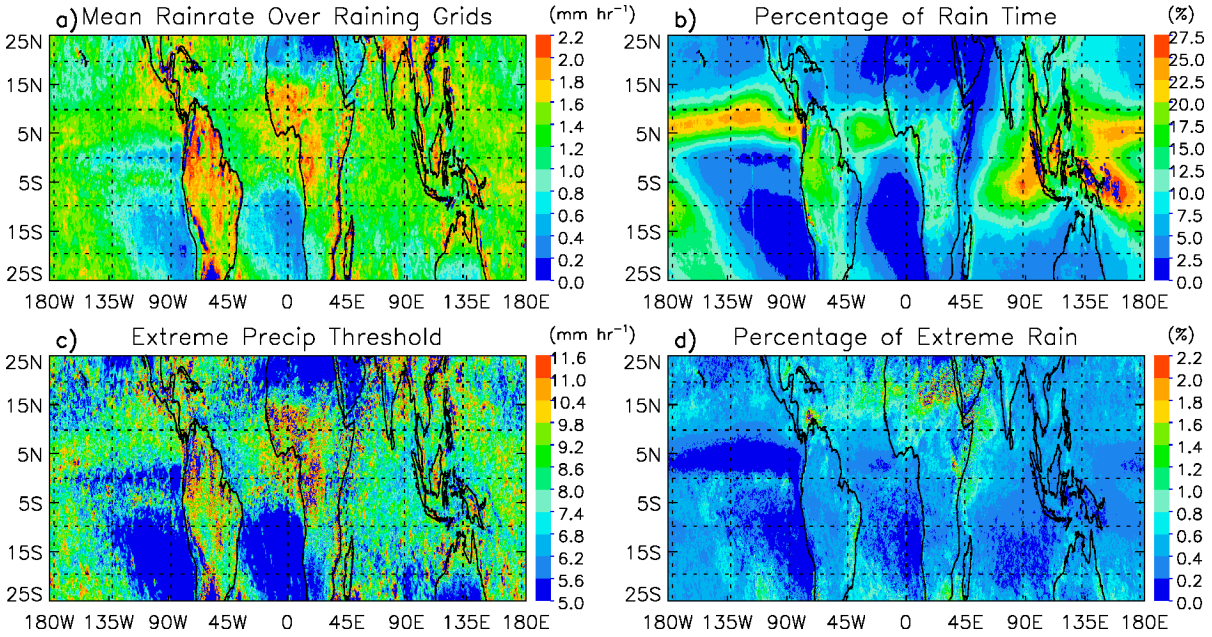

Figure 1. Geographic distribution of (a) mean rain rate (mm h^{-1}) for grids with instantaneous rain rates exceeding 0.01 mm h^{-1}, (b) percentage of time with rain rates exceeding 0.01 mm h^{-1}, (b) extreme precipitation threshold (mm h^{-1}) used to extract extreme precipitation events, and (d) percentage of time with extreme rain relative to all raining time. Statistics are based upon half-hourly, 0.1° x 0.1° IMERG data from July 2006 to June 2010.

760

761

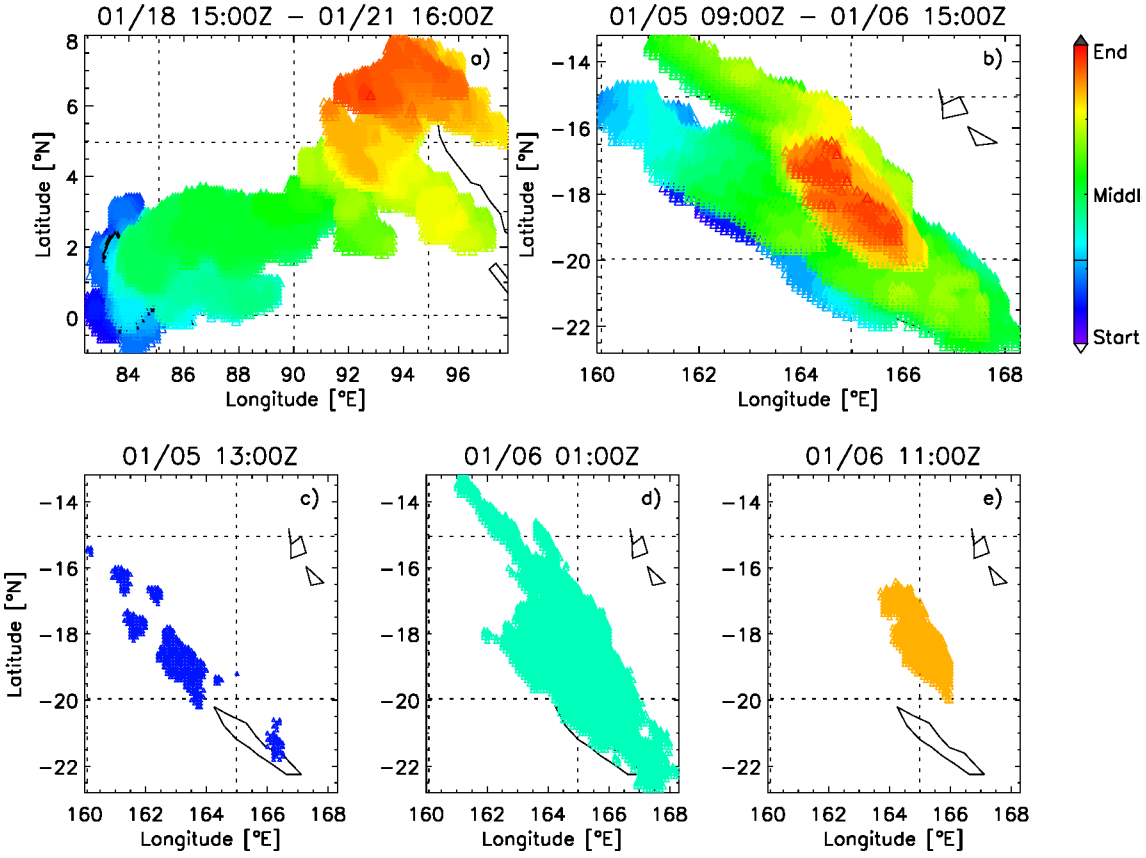

Figure 2. Examples of two extreme precipitation events on (a) January 18-21 and (b) January 5-6, 2007. Panels (c), (d), and (e) show the early stage, the peak stage with maximum areal coverage, and the near-end stage of the second event, respectively. Color represents the progression of the EPE from start (blue) to peak (green) to delay (red).

762

763

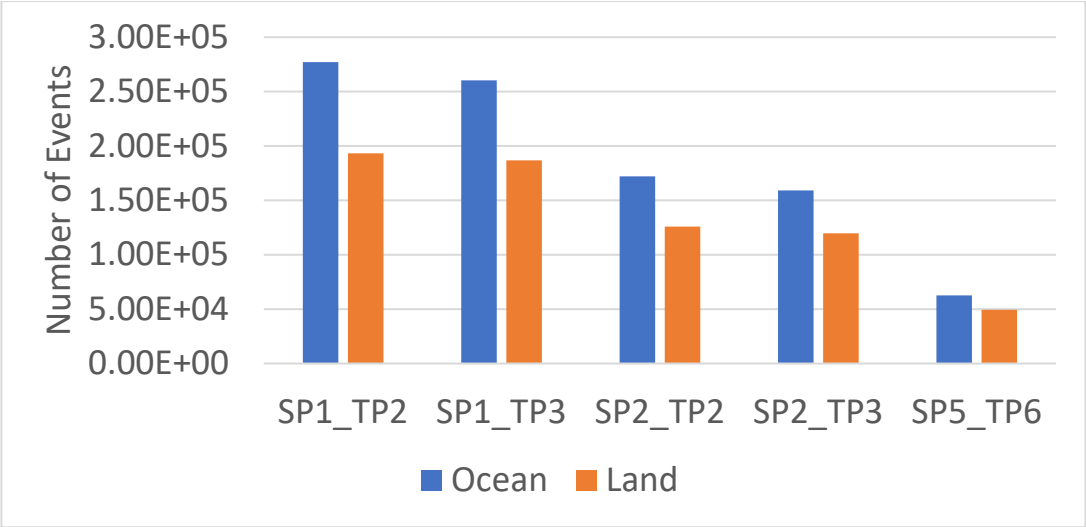

Figure 3. Total numbers of extreme precipitation events (EPEs) from January, April, July and October 2007 over tropical land (orange) and oceanic (blue) regions for five combinations of spatial (SP=1, 2, and 5 grid units of 0.1° ×0.1° grids) and temporal (TP=2, 3, and 6 h) gaps.

764

765

766

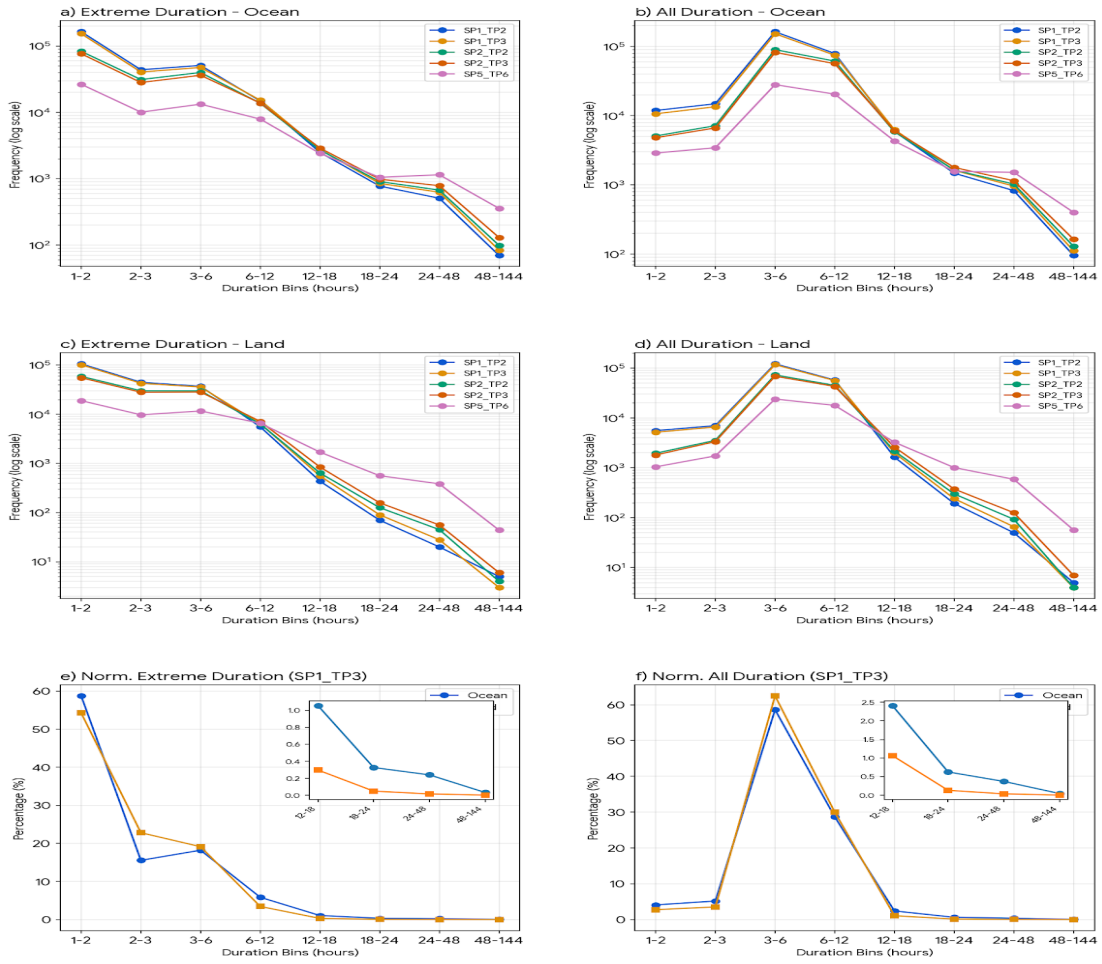

Figure 4. Number of extreme precipitation events (EPEs) with different spatial–temporal gaps, stratified by extreme duration (left column) and event duration (right column). Panels (a,b) show results over tropical oceans, and panels (c,d) show results over tropical land. Panels (e,f) present the percentage distribution of event durations for the SP1–TP3 case over ocean and land, respectively, normalized by the total number of events. Event duration may exceed extreme duration by up to 2 hours because the detection algorithm allows a 2-hour gap between extreme and light-rain grids.

767

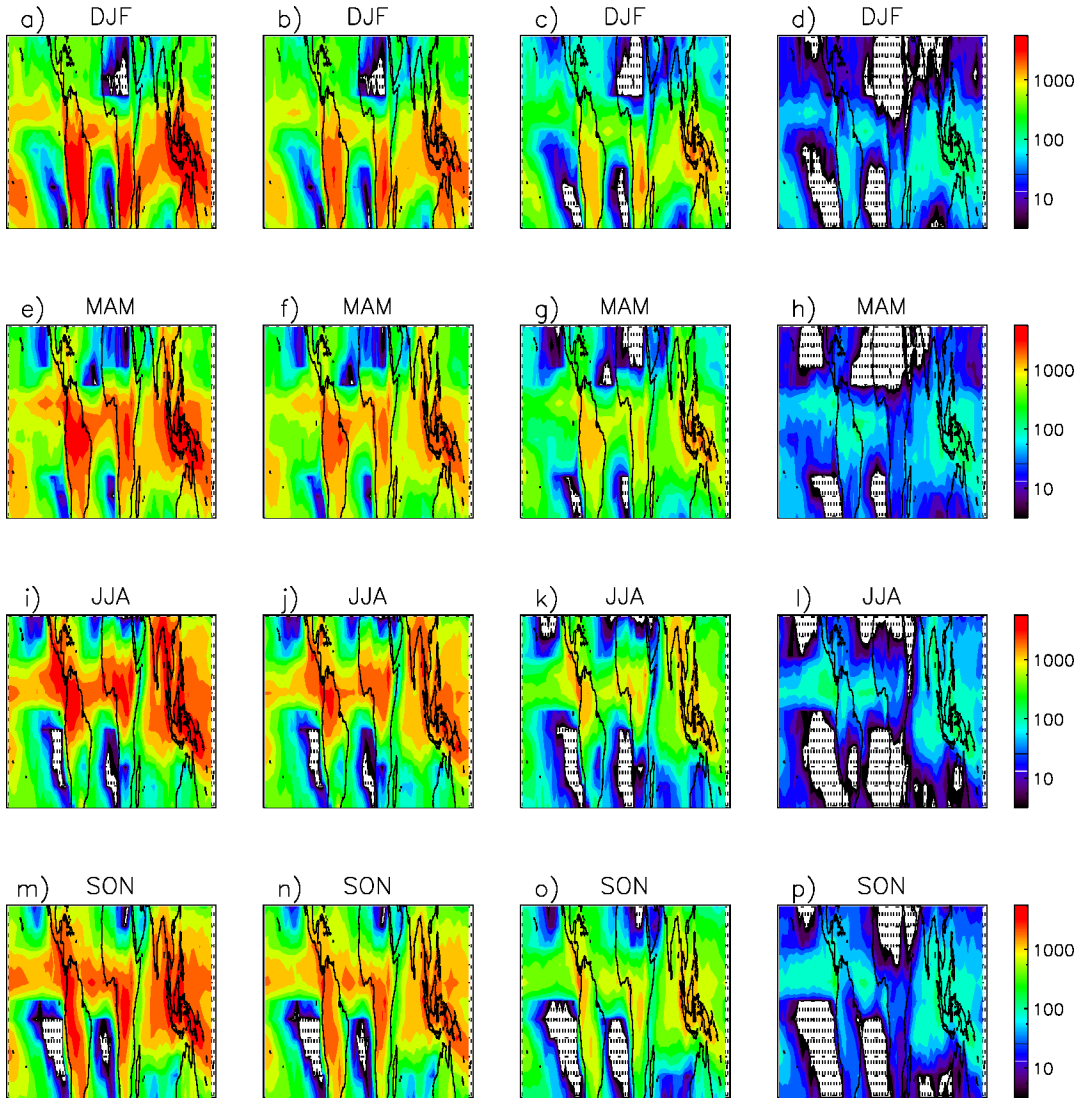

768 **Figure 5.** Geographic distribution of extreme precipitation events (EPEs) for all durations (1st
769 column), durations shorter than 6 h (2nd column), durations of 6–12 h (3rd column), and
770 durations longer than 12 h (4th column), shown for four seasons: DJF (1st row), MAM (2nd
771 row), JJA (3rd row), and SON (4th row)

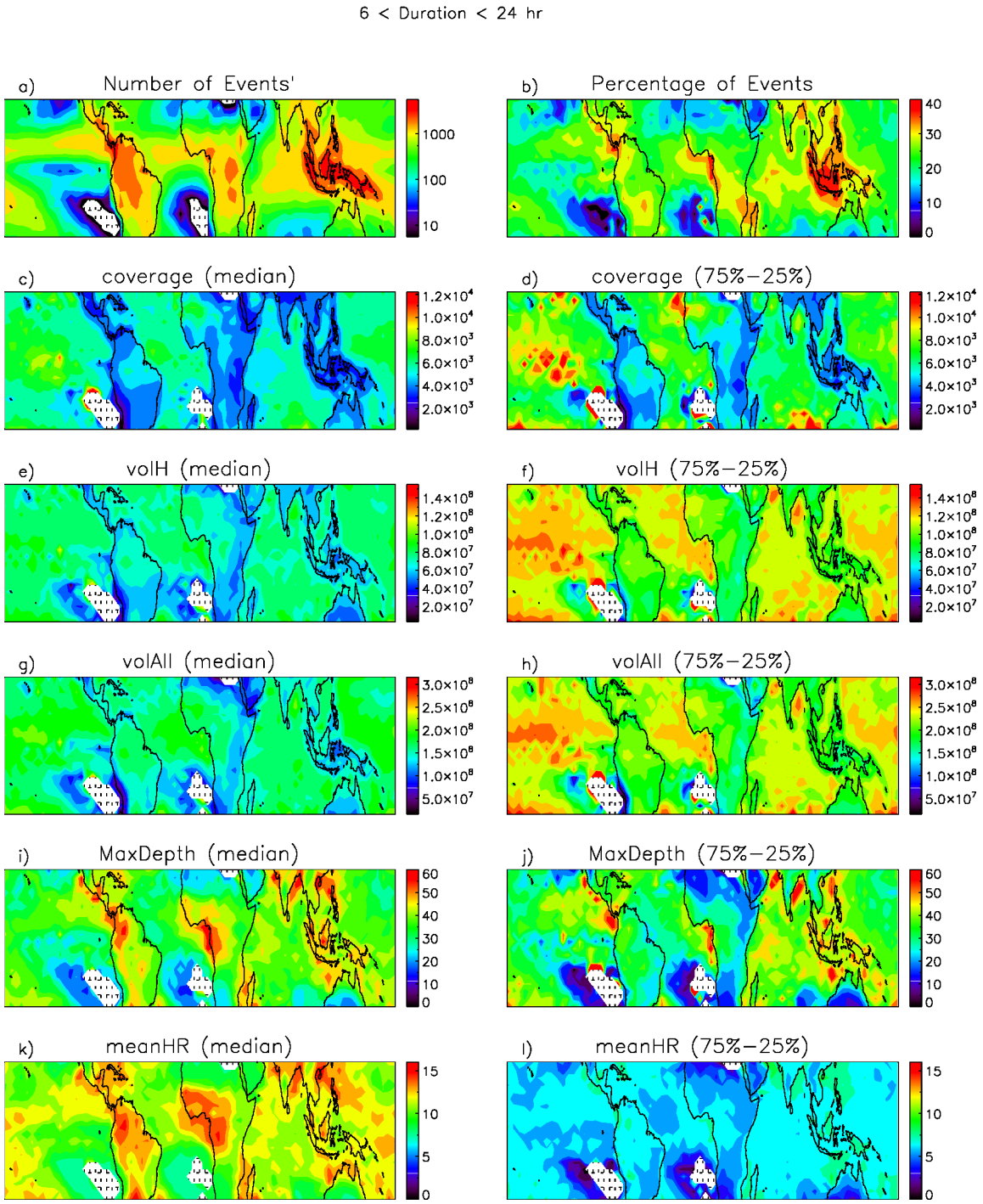

772

773 **Figure 6**. Spatial distribution of the number of events (a), percentage of events (b), IQR (75% -

774 25% range) of EPE event parameters including areal coverage (c, d), extreme rainfall (volH, e, f)

775 and total rainfall (volAll, g, h), maximum depth (MaxDepth, i, j), and mean extreme rain rate

776 (meanHR, k, l) for events with durations between 6 and 24 hours.

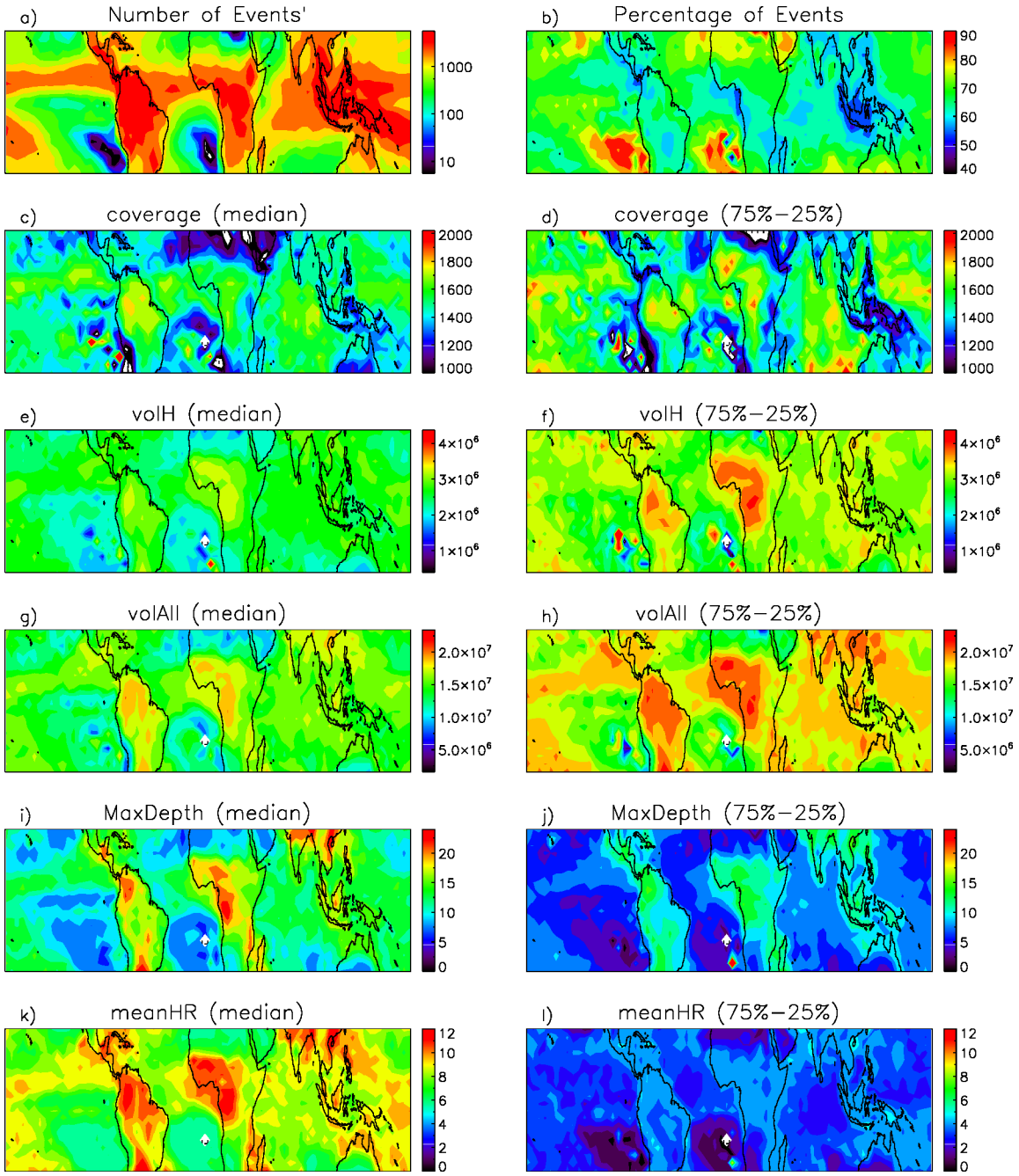

777

778

779 **Figure 7.** Same as Figure 6 but for events with 1-6 h durations.

780

781

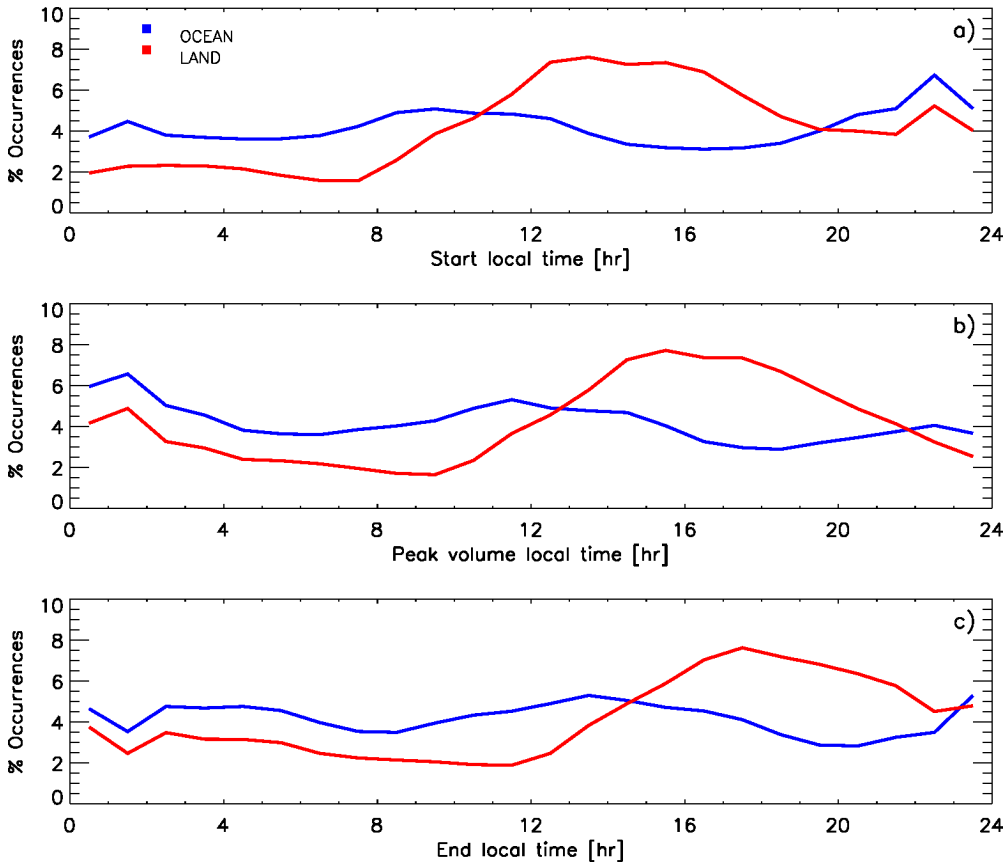

Figure 8. Diurnal variation of percentage of events occurring in each hour of the day for start (a), peak-volume (b), and end (c) times (blue for ocean and red for land).

790

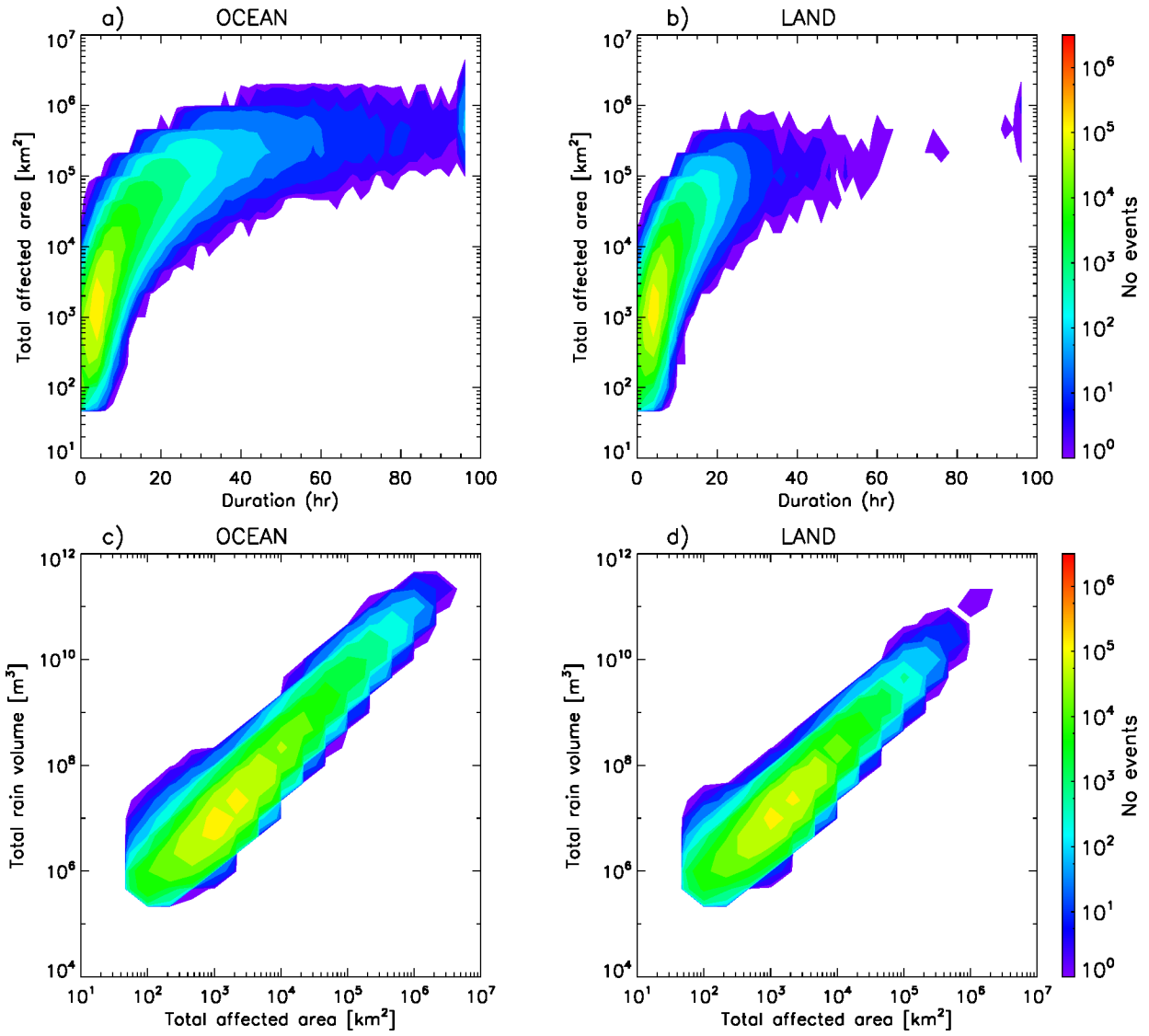

Figure 9. Number of occurrences of areal coverage (total affected area) vs. event duration (top two plots), and total rainfall vs. areal coverage (total affected area; bottom two plots). The left two plots are for ocean while the right two plots are for land.

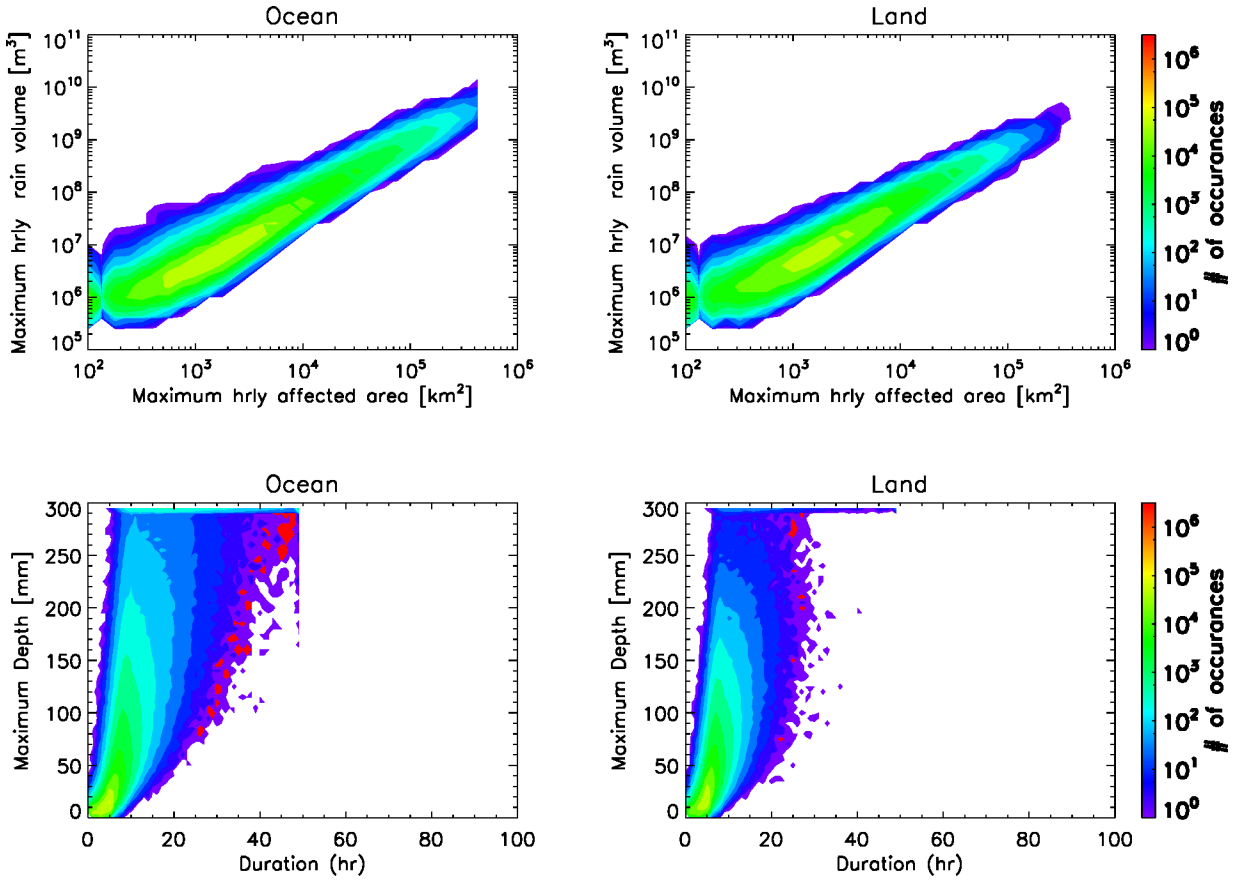

Figure 10. As in Figure 9, but showing the relationships between maximum hourly areal coverage (affected area) and maximum hourly rainfall (top two plots), and between event duration and maximum depth (bottom two plots). The left two plots are for ocean while the right two plots are for land.

791

792